

Damage Detection of the 2011 Tohoku, Japan Earthquake from High-resolution SAR Intensity Images



W. Liu & F. Yamazaki

Chiba University, Japan

H. Gokon & S. Koshimura

Tohoku University, Japan

SUMMARY:

The Tohoku earthquake of March 11, 2011, caused gigantic tsunamis and widespread devastation. Various high-resolution satellites quickly captured the details of affected areas, and were used for emergency response. In this study, high-resolution pre- and post-event TerraSAR-X intensity images were used to identify damaged buildings. Since the damaged buildings show changes in backscatter intensity, they can be detected by calculating the difference and correlation coefficient. A GIS map was introduced to identify individual damaged buildings and investigate their characteristics. The results were compared with a visual interpretation of the area, which confirmed that the proposed method was highly accurate.

Keywords: TerraSAR-X intensity image, Tsunami, Building, Damage detection

1. INSTRUCTIONS

The Tohoku earthquake of March 11, 2011, was the most powerful earthquake to hit Japan since modern record-keeping began in 1900. The epicentre was located at 38.322° N, 142.369° E at a depth of about 32 km. The earthquake triggered extremely high tsunamis of up to 40.5 m run-up in Miyagi, Iwate Prefecture, and caused huge loss of human lives and destruction of infrastructure. According to the Geospatial Information Authority of Japan (GSI), areas totalling approximately 561 km² were flooded by tsunamis following the earthquake (GSI, 2011). The earthquake resulted from a thrust fault on the subduction zone plate boundary between the Pacific and North American plates. According to the GPS Earth Observation Network System (GEONET) operated by GSI in Japan, crustal movements exceeded 5.3 m horizontally, and 1.2 m vertically over wide areas of the Tohoku region. It is recognized that remote sensing is an efficient tool to monitor a wide range of natural events by optical and radar sensors. Although optical images can easily capture detailed ground surface information, the approach is limited by weather conditions. In contrast, synthetic aperture radar (SAR) sensing is independent of weather and daylight conditions, and thus more suitable for mapping damaged areas reliably and promptly. Due to remarkable improvements in radar sensors, high-resolution COSMO-SkyMed and TerraSAR-X (TSX) SAR images are available with ground resolution of 1 to 5 m, providing detailed surface information.

SAR images have also been used in interferometric analysis to investigate damage to buildings (Ito *et al.*, 2000; Yonezawa and Takeuchi, 2001). Matsuoka and Yamazaki (2004) performed a feasibility study on backscattering characteristics of damaged areas in the 1995 Kobe, Japan earthquake, and developed an automated method to detect hard-hit areas using ERS/SAR intensity images. The proposed method was also applied to Envisat/ASAR images in the 2003 Bam, Iran earthquake (Matsuoka and Yamazaki, 2005). Recently, several studies attempted to detect damage at the scale of a single building unit, using both high-resolution optical and SAR images (Brunner *et al.*, 2010; Wang and Jin, 2012).

In this study, one pre-event and two post-event TSX intensity images were used to identify damaged

buildings following the Tohoku tsunami. The washed buildings were distinguished by changing backscattering intensity. A GIS map was then introduced to identify individual damaged buildings within the flooded areas (Gokon and Koshimura, 2012). Finally, the accuracy of the proposed method was assessed through comparison with the GIS map.

2. SAR INTENSITY IMAGES AND PREPROCESSING

This study focuses on the coastal zone of Tohoku, Japan, shown in Fig. 2.1(a), which was most severely affected in the 2011 Tohoku earthquake. Three TerraSAR-X images, taken before and after the earthquake (shown in Fig. 2.1(b–d)) were used to detect the damaged buildings. The pre-event image was taken on October 21, 2010 with 37.3° incident angle, and two post-event images were taken on March 13 (two days after the earthquake) and March 24, 2011, with the same incidence angle at the centre of the images. Those images were captured with HH polarization and in a descending path. The images were acquired in the StripMap mode, and thus both the azimuth and ground range resolutions were about 3.3 m. We used the orthorectified multi-look corrected products (EEC) provided by DLR, where the image distortion caused by a variable terrain height was compensated for by using a globally available DEM (SRTM). The products were provided in the form projected to a WGS84 reference ellipsoid with a resampled square pixel size of 1.25 m.

Two preprocessing approaches were applied to the images before extracting damaged buildings. First, the three TSX images were transformed to a Sigma Naught (σ^0) value, which represents the radar reflectivity per unit area in the ground range. After the transformation, the backscattering coefficients of the images were between -35 dB and 25 dB. Then, an enhanced Lee filter (Lopes *et al.*, 1990) was applied to the SAR data to reduce the speckle noise. To minimize the loss of information contained in the SAR intensity images, the window size of the filter was set as 3×3 pixels.

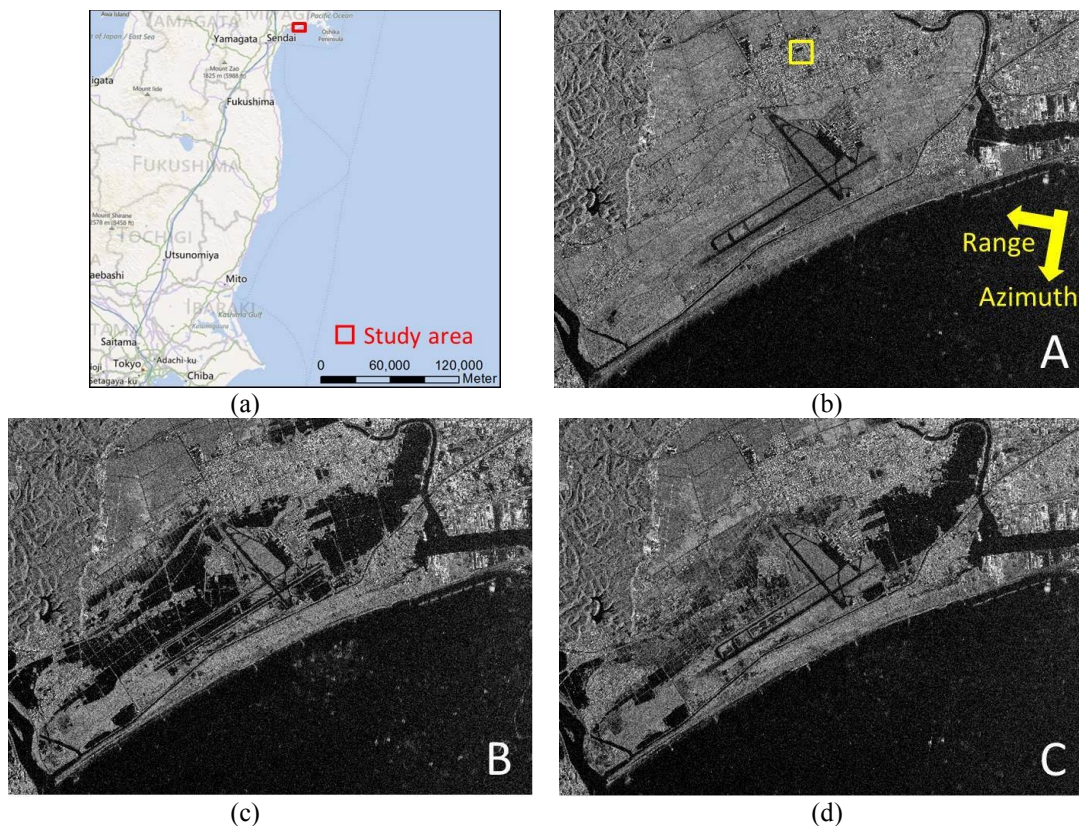


Figure 2.1. Study area along the Pacific coast of Tohoku, Japan (a); the pre-event TSX image taken on Oct. 21, 2010 (b); and the post-event images taken on March 13, 2011 (c), and on March 24, 2011 (d).

3. CRUSTAL MOVEMENT

Since the TSX images used in this study were geo-coded by the GPS orbit determination to a high level of accuracy (Breit *et al.*, 2010), the displacements between the pre- and post-event TSX images were mostly caused by crustal movements due to the earthquake. A part of colour composite image in the frame of Fig. 2.1(b) is shown in Fig. 3.1(b), where the pre-event images were loaded as Green and Blue colours while the post-event image on March 13, 2011, as Red colour. The outlines of buildings in Fig. 3.1(a) are seen to be shifted from Cyan to Red colours. These displacements were used to detect crustal movements (Liu and Yamazaki, 2012), but they will cause errors when detecting changes associated with damaged buildings in this study.

According to records from the Yamoto GPS ground station in the study area which is shown in Fig. 3.1(a), 4.09 m southeast horizontal and 0.52 m downward movements were observed until March 12, 2011, as shown in Fig. 3.2. Affected by the earthquake, the GPS station stopped operation for several days. The three-dimensional surface displacements recorded at the GPS station were converted to the two-dimensional displacements in the TSX images considering the side-looking observation mode of SAR, which are 3.24 m to the east and 1.06 m to the south, while that on March 24 was 3.42 m to the east and 1.12m to the south. Then the pre-event TSX image was manually shifted 3 pixels (3.75 m) to the east (to the right as viewed by an on-screen user) and 1 pixel to the south (to the down) in order to match the post-event TSX images; the two temporal shapes of buildings were then almost overlapped in the new colour composite, shown in Fig. 3.1(c).

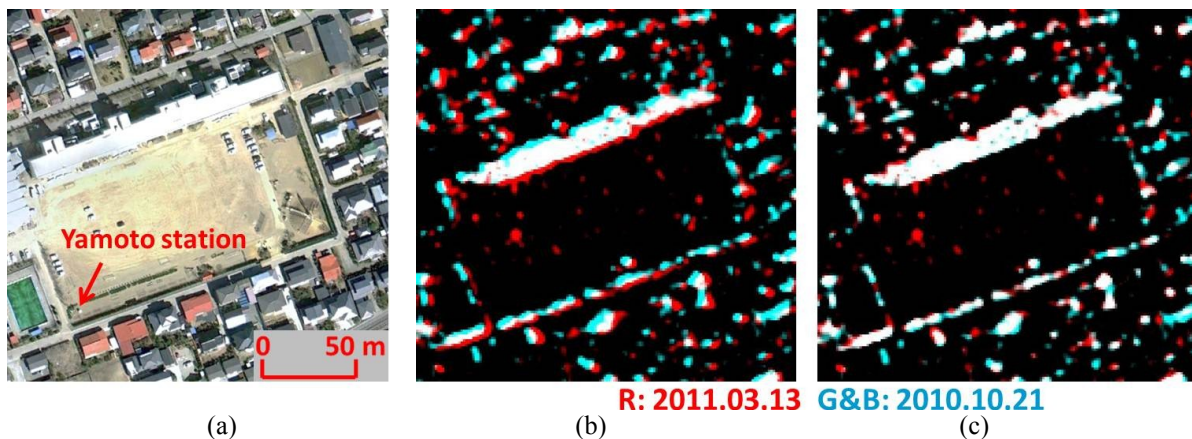


Figure 3.1. Aerial photographs taken on April 6, 2011 over the yellow frame of Figure 1(b), obtained from Google Earth (a); the color composite of the original pre- and post-event (March 13) TSX intensity images (b); and the shifted pre- and post-event composite image (c).

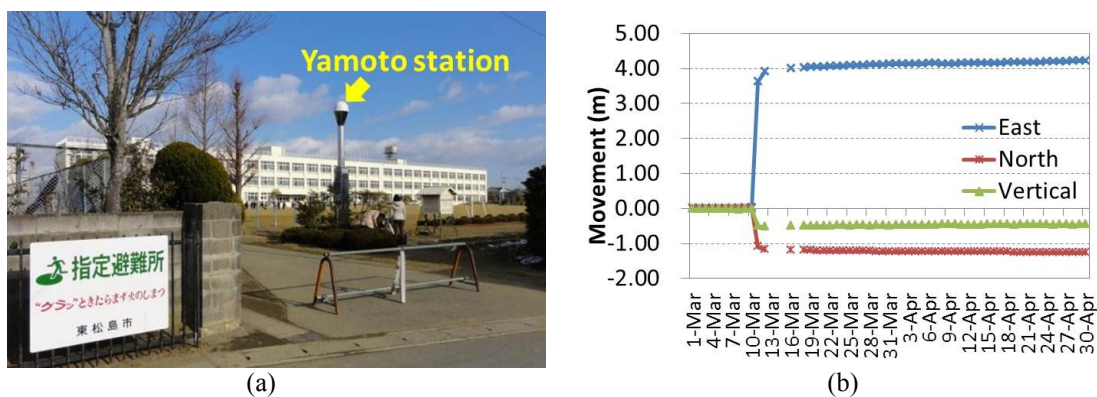


Figure 3.2. Photograph of field survey around Yamoto GPS ground station taken on Jan. 13, 2012 (a); the observed 3D movements at Yamoto station from March 1 to April 30, 2011, where the reference value (zero) is data for Oct. 21, 2010 (b).

4. DETECTION OF DAMAGED BUILDINGS

Numerous buildings were demolished and washed away by the huge tsunami of more than 10 m, and hence it was difficult to observe damaged buildings individually in field surveys, due to widespread destruction. Therefore, a method was proposed to extract damage for each building unit, using high-resolution pre- and post-event TSX intensity images and a GIS map of buildings produced by Gokon and Koshimura (2012), shown in Fig. 4.1(a).

4.1. Calculation of a change factor

The backscattering coefficients for damaged buildings show both increasing and decreasing trends, depending on the damage status. Additionally, the backscattering coefficients for no-change (undamaged) buildings have very high correlation between the pre- and post-event TSX images. Hence, we took advantage of these features to detect damaged buildings using a change factor that includes both the difference and correlation coefficient (Liu and Yamazaki, 2010). The change factor between the pre-event image and the post-event image on March 13, 2011, is termed z_1 , while that between the pre-event image and the image on March 24, 2011, is termed z_2 . The two change factors were calculated by Eqn. 4.1, and are shown in Fig. 4.2.

$$z = \frac{|d|}{\max|d|} - c \cdot r \quad (4.1)$$

where

$$d = \bar{I}b - \bar{I}a \quad (4.2)$$

$$r = \frac{N \sum_{i=1}^N I_{a_i} I_{b_i} - \sum_{i=1}^N I_{a_i} \sum_{i=1}^N I_{b_i}}{\sqrt{\left(N \sum_{i=1}^N I_{a_i}^2 - \left(\sum_{i=1}^N I_{a_i} \right)^2 \right) \left(N \sum_{i=1}^N I_{b_i}^2 - \left(\sum_{i=1}^N I_{b_i} \right)^2 \right)}} \quad (4.3)$$

where $\max(|d|)$ is the maximum absolute value of the difference of the backscattering coefficients; c is the weight between the difference and the correlation coefficient, to be determined between 0.0 and 1.0; I_{a_i} and I_{b_i} are the backscattering coefficients of i -th pixel of the pre- and post-event images, while \bar{I} is the average value; and $N (= k \times k)$ is the window size.

The window size to detect damaged buildings was set as 5×5 pixels (about 40 m^2) considering to the building size. Since the correlation coefficient is very sensitive to subtle changes, it showed a low value even when no large change had occurred. Conversely, the normalized absolute value of the difference was relatively stable. Hence, in this study, the weight for the correlation coefficient was set as half of that for the difference, which is 0.5; as a result, the value of the z -factor then lies between -0.5 and 1.5, where a high value indicates high probability of change. In Fig. 4.2, the change factors for flooded areas are highest, displayed in Red colour, while the factors for north urban areas are lowest, displayed in Blue colour.

4.2. Building height

Building damage can be detected by the amount of change in a building's outline. However, the outlines of buildings in the GIS map did not match those in the TSX images, due to the side-looking nature of SAR. A building in a TSX image shows layover from the actual position to the direction of the sensor, as shown in Fig. 4.3(a). The layover is proportional to the building height, as in Eqn. 4.4.

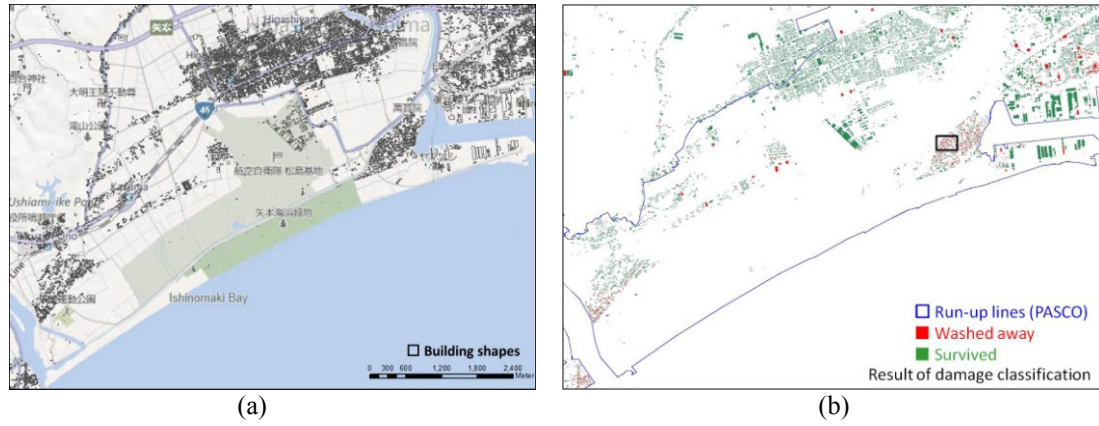


Figure 4.1. A GIS map of buildings incited from Gokon and Koshimura (2012) (a); result of damage classification using factor z_1 and z_2 (b).

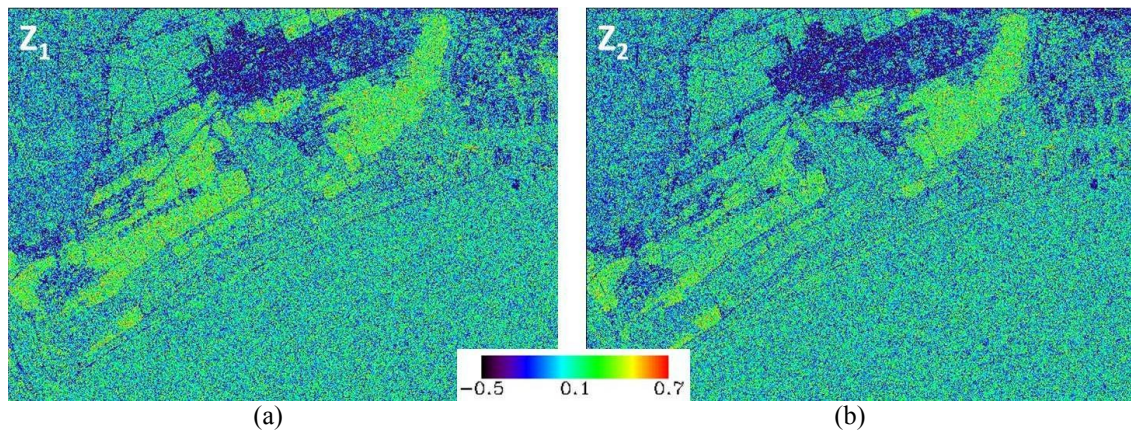


Figure 4.2. The change factor calculated from the pre-event image and the post-event image taken on March 13, 2011 (a), and the image taken on March 24, 2011 (b).

$$L = H / \tan \theta \quad (4.4)$$

where θ is the incident angle of the TSX image.

Fig. 4.3(b) shows the outlines of buildings over the pre-event (Oct. 21, 2010) images. The walls of a building, which show highest backscatter due to the corner reflection, are outside the outline in the GIS map. In this case, the building cannot be detected as damaged even when large change occurs to its walls. Therefore, the GIS map was shifted to the direction of the SAR sensor (southeast) in order to match the TSX images. Since height data for buildings was not available, all the building shapes were shifted against to the range direction respectively, to match with the pre-event TSX image. According to the location information, most of the buildings in the study area were two stories. Hence, the buildings' heights were assumed as all below or equal to 12 m (four stories). Then the relationship between the building's height and the length of layover was obtained as Table 4.1, according to the 37.3° incidence angle and the 190.4° path angle (clockwise from the north). The building shapes were shifted as the height increasing per meter, and the total value of the backscatter intensities in the pre-event TSX image within the shifted building shape was calculated respectively. The building's height was estimated when the total value of the backscatter got to the maximum. Finally, the new building outlines, after shifting, were plotted on the pre-event TSX image, as shown in Fig. 4.3(c). The possible buildings' heights were also obtained, as shown in Fig. 4.4(a).

The buildings were also classified by the number of stories, as shown in Fig. 4.4(b). Since most of the housings in the target area have gable roofs, the heights are higher than 3 m (height per story) multiply to the number of stories. Then the buildings with the height below 6 m were classified as

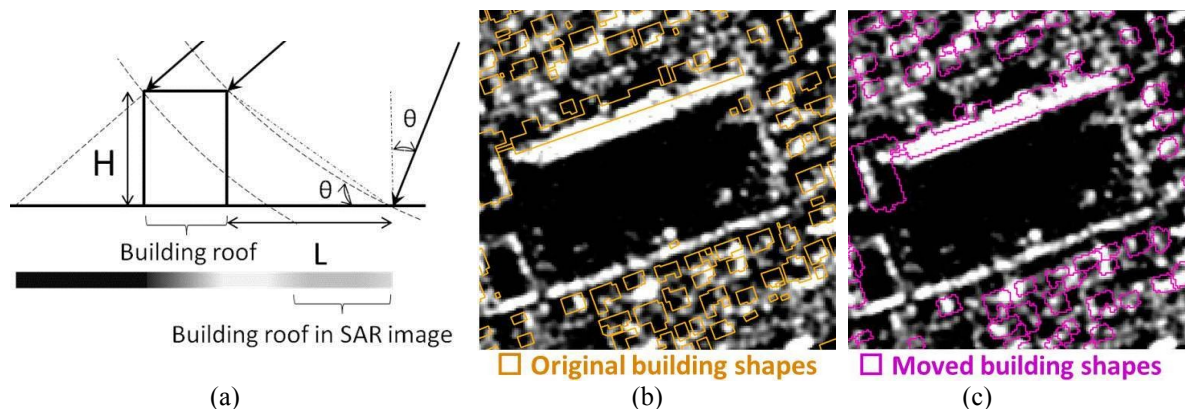


Figure 4.3. Simulation of the location of a building in a SAR image (a); the GIS map of buildings over the pre-event TSX images at the same area of Figure 2(b); and the modified result after shifting the GIS map (c).

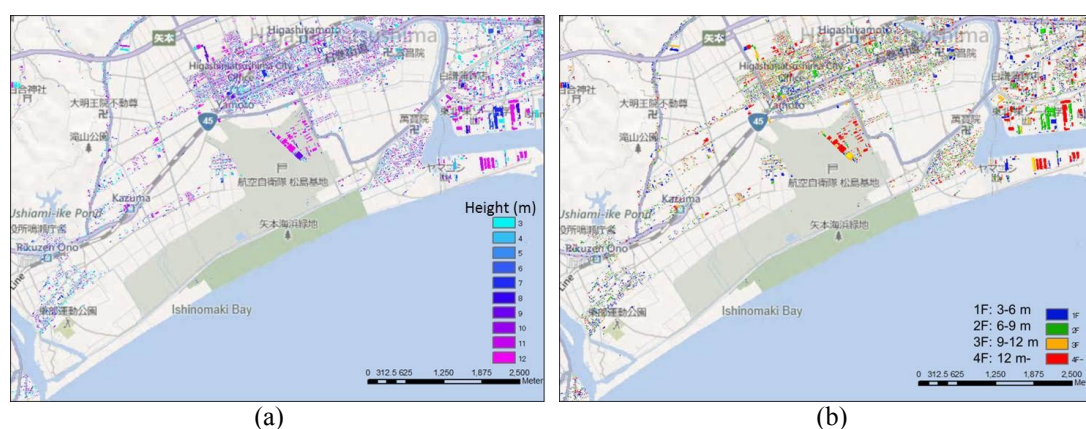


Figure 4.4. A GIS map of estimated buildings' height (a) and number of stories (b)

Table 4.1. Relationship between the building's height and the length of layover

		Height (m)										
			3	4	5	6	7	8	9	10	11	12
Layover	Length (m)	Total	3.94	5.25	6.56	7.88	9.19	10.50	11.81	13.13	14.44	15.75
		East	3.88	5.17	6.46	7.76	9.05	10.34	11.63	12.93	14.22	15.51
		North	-0.68	-0.91	-1.14	-1.37	-1.60	-1.82	-2.05	-2.28	-2.51	-2.74
	Shift (pixel)	East	4	5	6	7	8	9	10	11	12	13
		North	-1	-1	-1	-2	-2	-2	-2	-2	-3	-3

one story, below 9 m as two stories, below 12 m as three stories and equal to 12 m as four stories. From Fig. 4.4(b), several large buildings can be seen as four stories, which are plants. Although most of these buildings are only two stories, the heights of them are close to 12 m and classified into four stories. The accuracy of the building height should be discussed in the future study. However, compared with Fig. 4.3(b), larger areas of high backscattering intensities were located within the new building outlines.

4.3. Damage detection

Firstly, the damage detection of buildings was carried using only z_1 . Since a high value of factor indicates high probability of change, a building with an average factor value greater than 0 within its outline is considered as damaged. Considering to the limitation of the resolution and the window size which was used to calculate the factor, the buildings with the area smaller than 25 pixels (about 40 m²) were removed from the targets. Part of buildings in the frame of Fig. 4.1(b) categorized as damaged is shown in Fig. 4.5(a), using the change factors for March 13. Comparison with aerial photographs taken before and after the earthquake, shown in Fig. 4.5(c–d), confirmed that buildings that were

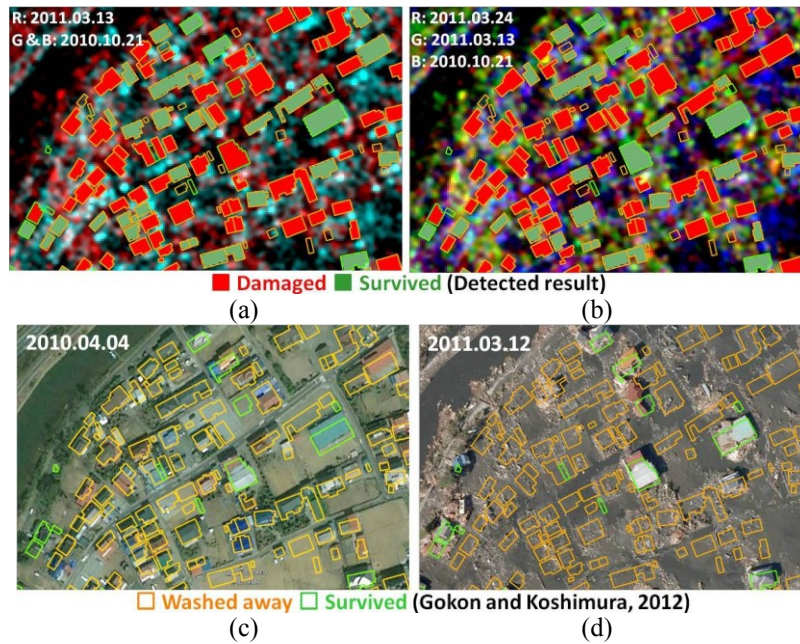


Figure 4.5. Result of damage detection using only factor z_1 (a) and the average of z_1 and z_2 (b); result of visual interpretation by Gokon and Koshimura (2012) overlying the pre- and post-event aerial photographs (c-d).

completely washed away were detected successfully. However, some extensively damaged buildings where debris remained at the same position could not be detected, due to the small change in backscatter. From the TSX image taken on March 24, 2011, some of these buildings became distinguishable due to the ongoing removal of debris. Thus, both the z_1 and z_2 factors were used to detect damaged buildings in this study. A new factor was calculated by getting the average of the two factors. Then a building was classified as damaged if the averaged value for the new factor was greater than 0. The results are shown in Fig. 4.1(b). The part in the frame is shown in Fig. 4.5(b), which shows better match with visual interpretation than Fig. 4.5(a).

5. VERIFICATION AND DISCUSSION

To verify the accuracy of the detected result, the building damage map produced by Gokon and Koshimura (2012) was introduced as a reference. There are more 10-thousand buildings in the study area, and 8573 buildings within the run-up lines. The accuracy of the result was evaluated by both the pixel-base and building unit-base. When the result was evaluated by pixel-base, the overall accuracy in the study area was 93%, with producer accuracy of 62% and user accuracy of 69% for the damaged buildings. When the result was evaluated by building unit-base, the overall accuracy was 91%, producer accuracy was 64% and user accuracy was 64%. Since several buildings, which were located out of the run-up area and removed due to ordinary demolition, were categorized as damaged, the accuracy within the run-up lines was also evaluated, as shown in Table 5.1. Then the overall accuracy evaluated by the pixel-base was 92%, while it was 90% by building unit-base. Although the overall accuracies within the run-up lines were lower than that were evaluated within the all study area, the producer accuracies for damaged buildings became higher.

There are two reasons for classification errors in the detection process. The first is the discrepancy between the real locations of buildings and those in the TSX images. Although all the buildings in the study area were shifted according to their speculated height, there are still several buildings were not matched with the TSX image. Thus, some damaged buildings of these types were categorized wrong. Additionally, some undamaged buildings located within the flooded areas were misclassified as damaged. The second reason is the influence of debris. As shown in Fig. 4.5, some washed-away buildings with debris left at the original locations could not be detected correctly.

The relationship between the building size and the fragility within the run-up lines was investigated, and shown in Fig. 5.1. The buildings with the size around 100 m² were the most popular in the study area, and accounted as 55% of all buildings. The buildings with the size larger than 1000 m² were the green houses and the plants. The percentage of damaged building per hierarchy was calculated by Eqn. 5.1.

$$P_D\% = \frac{\text{Number of the damaged buildings}}{\text{Number of buildings}} \times 100 \quad (5.1)$$

When the building is smaller than 300 m², the $P_D\%$ keep constant and around 20%. When the building is larger than 300 m², the $P_D\%$ gets down as the size goes larger. However, the $P_D\%$ for the buildings which are larger than 1000 m² became higher due to fragility of the green houses and the plants. 85% of the damaged buildings are smaller than 200 m², which means small buildings are washed away easily.

Table 5.1. Accuracy of damage detection evaluated by pixel-base (a) and building unit-base (b) methods within the run-up lines.

		(a)				(b)					
		Building Damage Map (%)				Building Damage Map					
pixel-base		Washed away	Survived	Total	U. A.	Building unit-base		Washed away	Survived	Total	U. A.
Detected result	Damaged	7.9	4.4	12.4	64.2	Detected result	Damaged	820	400	1220	67.2%
	Survived	3.7	84.0	87.6	95.8		Survived	471	6882	7353	93.6%
	Total	11.6	88.4	100.0			Total	1291	7282	8573	
	P. A.	68.5	95.0		91.9		P. A.	63.5%	94.5%		89.8%

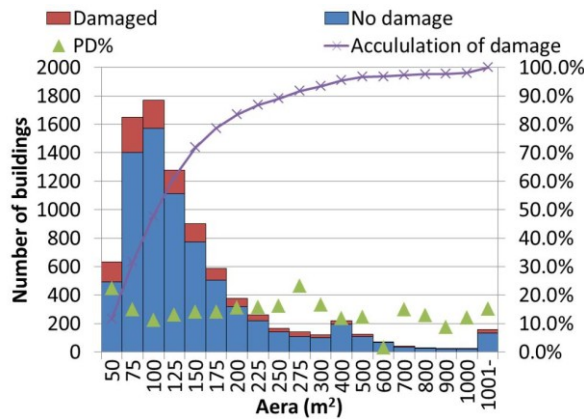


Figure 5.1. Relationship between the buildings' size and fragility.

6. CONCLUSIONS

In this study, damage following the 2011 Tohoku, Japan earthquake and tsunami was assessed using high-resolution TerraSAR-X intensity images taken before and after the earthquake. Damaged and washed-away buildings were detected from the changes of backscattering coefficients. The average value for the change factors in the outline of each building was calculated and used to judge the damage status of the building. The resulting classifications were compared with a GIS damage map produced by visual interpretation, showing that the proposed method achieved 90% overall accuracy. Thus, the proposed approach using high-resolution SAR images is considered reliable for use in emergency response following natural disasters. The proposed method also estimated the buildings height according to the length of layover in SAR images. Although the accuracy of the height estimation should be discussed using more images, it is used for urban planning and monitoring. The

damage status will be classified into finer classes using the change factors in the near future.

ACKNOWLEDGEMENT

The TerraSAR-X images used in this study were provided by PASCO Corporation, Tokyo, Japan, as one of the granted projects of the SAR data application research committee.

REFERENCES

- Breit, H., Fritz, T., Balss, U., Lachaise, M., Niedermeier, A. and Vonavka, M. (2010). TerraSAR-X SAR Processing and Products, *IEEE Transactions on Geoscience and Remote Sensing*, **48: 2**, 727-740.
- Brunner, D., Lemoine, G. and Bruzzone, L. (2010). Earthquake damage assessment of buildings using VHR optical and SAR imagery, *IEEE Transactions on Geoscience and Remote Sensing*, **48: 5**, 2403-2420.
- Geospatial Information Authority of Japan (GSI), (2011). http://www.gsi.go.jp/BOUSAI/h23_tohoku.html.
- Gokon, H. and Koshimura S. (2012). Mapping of building damage of the 2011 Tohoku Earthquake Tsunami in Miyagi prefecture, *Coastal Engineering Journal*, **54:1**, 1250006-1-1250006-12.
- Ito, Y., Hosokawa, M., Lee, H. and Liu, J.G. (2000). Extraction of damaged regions using SAR data and neural networks, ISPRS2000, *International Activities of Photogrammetry and Remote Sensing*, **XXXIII:B1**, 56-163.
- Lopes, A., Touzi, R. and Nezry, E. (1990). Adaptive speckle filters and scene heterogeneity, *IEEE Transactions on Geoscience and Remote Sensing*, **28:6**, 992-1000.
- Liu, W. and Yamazaki, F. (2011). Urban change monitoring by from multi-temporal TerraSAR-X images, *Joint Urban Remote Sensing Event*, 277-280.
- Liu, W. and Yamazaki, F. (2012). Detection of crustal movement from TerraSAR-X intensity images for the 2011 Tohoku, Japan Earthquake, *IEEE Geoscience and Remote Sensing Letters* (accepted for publication).
- Matsuoka, M. and Yamazaki, F. (2004). Use of satellite SAR intensity imagery for detection building areas damage due to earthquake, *Earthquake Spectra*, **20**, 975-994.
- Matsuoka, M. and Yamazaki, F. (2005). Building damage mapping of the 2003 Bam, Iran, Earthquake using Envisat/ASAR intensity imagery, *Earthquake Spectra*, **21**, S285-S294.
- PASCO (2011). http://www.pasco.co.jp/disaster_info/110311/.
- Wang, T.L. and Jin, Y.Q. (2012). Postearthquake building damage assessment using multi-mutual information from pre-event optical image and postevent SAR image, *IEEE Geoscience and Remote Sensing Letters*, **9:3**, 452-456.
- Yonezawa, C. and Takeuchi, S. (2001). Decorrelation of SAR data by urban damages caused by the 1995 Hyogoken-Nanbu Earthquake, *International Journal of Remote Sensing*, **22:8**, 1585-1600.